20686

LUNAR RESPONSE TO THE TIME-VARYING INTER-

PLANETARY MAGNETIC FIELD AND APPLICATION

TO THE ALSEP MAGNETOMETER EXPERIMENT

November 8, 1968

Bellcomm, Inc.

955 L'Enfant Plaza North, S.W.

Washington, D.C. 20024

LUNAR RESPONSE TO THE TIME-VARYING INTER-

PLANETARY MAGNETIC FIELD AND APPLICATION

TO THE ALSEP MAGNETOMETER EXPERIMENT

November 8, 1968

W. R. Sill
J. L. Blank

BELLCOMM, INC.

TABLE OF CONTENTS

BELLCOMM, INC.

ABSTRACT

A model is developed to predict the lunar response to the time-varying interplanetary magnetic field. This model is applied to the interpretation of ALSEP magnetometer data. It is shown that, based on the theory, data from a single ALSEP magnetometer should be sufficient to calculate interior electrical conductivities up to a maximum of $\sim 5(\Omega\text{-m})^{-1}$. This appears adequate to discriminate between currently proposed hot and cold models for the lunar interior.

BELLCOMM, INC.

<div align="center">

LUNAR RESPONSE TO THE TIME-VARYING INTER-
PLANETARY MAGNETIC FIELD AND APPLICATION
TO ALSEP MAGNETOMETER EXPERIMENT

</div>

1.0 INTRODUCTION

The primary purpose of the ALSEP magnetometer experiment is to study the interaction of the solar wind with the moon, and thereby provide information on the electrical properties of the lunar interior. This report presents a theory for the response of the moon to the time-varying interplanetary magnetic field, and examines the applicability of the theory to the interpretation of ALSEP magnetometer data.

The study of the interaction of the solar wind with the moon has thus far been directed primarily to the case of a constant magnetic field, $\partial B/\partial t = 0$. In this case the problem may be viewed as that of a moving conductor in a uniform magnetic field. The current responsible for the induced field flows through the moon with the current paths closing in the solar wind plasma. The magnitude of the induced field depends upon the characteristic electrical conductivity of the moon for this interaction, namely that of the lunar crust. The absence of an interaction on the sunlit side of the moon (Colburn et al., 1967) implies that the energy density of this induced magnetic field is much less than the directed kinetic energy density of the solar wind. By a calculation similar to that of Dessler (1967), this disparity in energies can be used to compute an upper bound for the conductivity of the lunar crust. The result is $\sigma < 10^{-5}$ $(\Omega\text{-m})^{-1}$. To determine the electrical conductivity of the lunar interior we must proceed to a consideration of time-varying magnetic fields.

The response of the moon to the time-varying interplanetary field is governed by eddy currents which flow in the lunar interior. The strength of the magnetic field induced by these currents provides a measure of the interior electrical conductivity of the moon. The time scale for decay of eddy currents is the Cowling time $\tau_c = \mu\sigma L^2$, where L is the characteristic dimension of the conductor. Therefore the response of

the moon to interplanetary magnetic field variations of periods $T \sim \tau_c$ provides the most sensitive measure of the electrical conductivity of the lunar interior. The Cowling times for various models of the lunar interior range from a few tenths of a day to thousands of days. The maximum power in the interplanetary magnetic field spectrum occurs at periods associated with field reversals, which fall within this range of possible Cowling times. Thus the understanding of the lunar response to these magnetic field variations appears to be an attractive method for determining the lunar interior conductivity. Knowledge of the conductivity would also provide information on the temperature of the lunar interior.

2.0 FORMULATION

2.1 Sector Structure and Power Density Spectrum of the Interplanetary Field

Except for periods when it is in the geomagnetic tail, the moon is imbedded in the solar wind and experiences the time-varying interplanetary magnetic field. There exist fluctuations of the interplanetary field due to many sources, e.g., waves and turbulence. We are principally concerned with those fluctuations caused by the corotation of the sector structure of the interplanetary magnetic field with the sun. Figure 2.1 shows schematically the sector structure as reported by Wilcox and Ness (1965). In the positive sectors the field is directed outward from the sun along an Archimedes spiral. At the orbit of the earth the interplanetary field lies predominately in the ecliptic plane, and the angle between the field vector and the radius vector from the sun is approximately 45°. This entire structure corotates with the sun in a period of about 27 days, and the pattern (number and size of the sectors) is relatively stable over at least several solar rotations. Simultaneous measurements of the field by two spacecraft separated by 1.3×10^6 km show a high degree of correlation, with a time lag corresponding to the time necessary to rotate the field pattern from one observation point to the other (Ness, 1966). Thus, at least for separations $\lesssim 10^6$ km, measurements at one point can be used to predict the field configuration at another point by
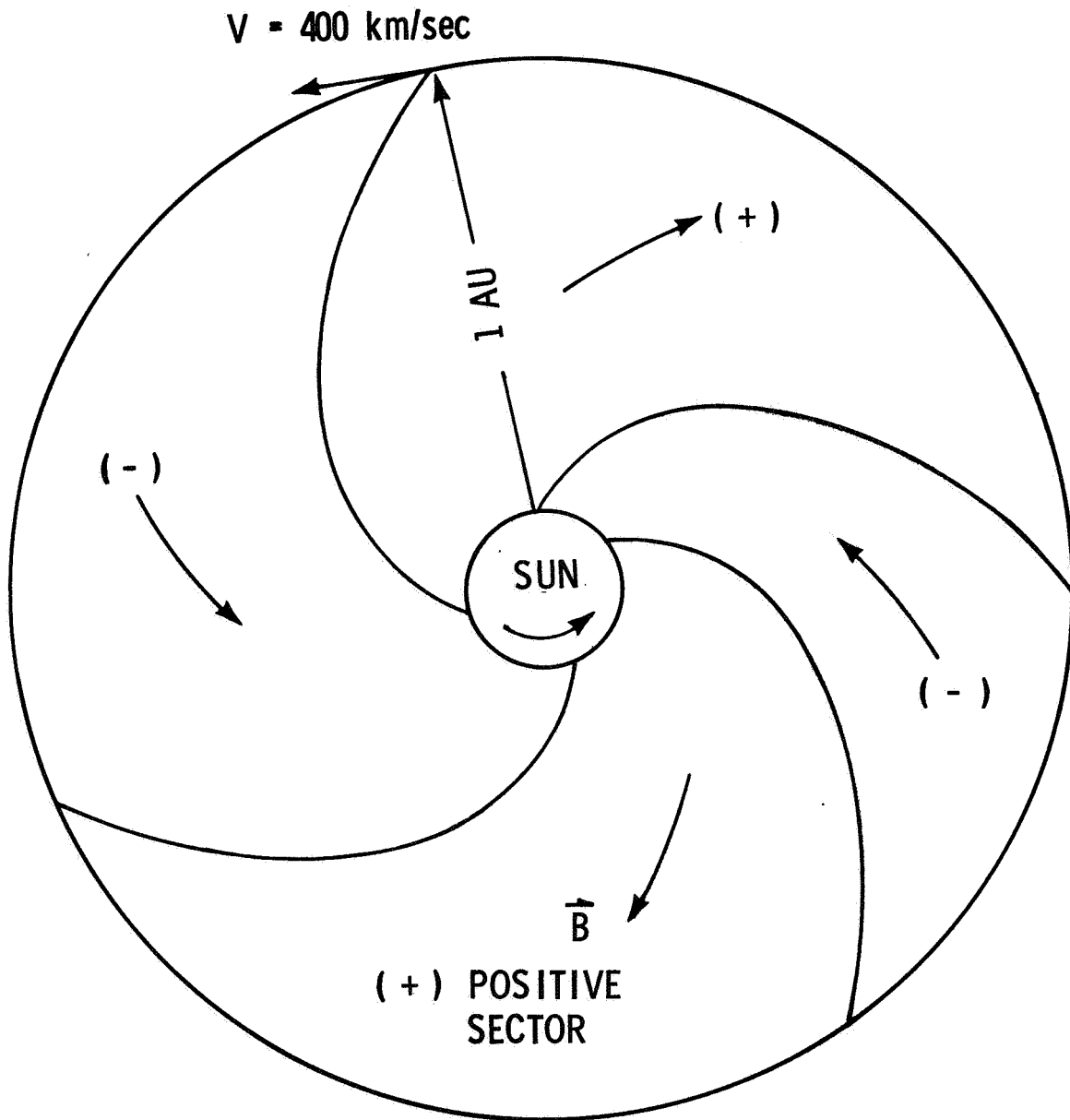
V = 400 km/sec

FIGURE 2.1 – SCHEMATIC ILLUSTRATION OF THE INTERPLANETARY
MAGNETIC FIELD SECTOR STRUCTURE

assuming that the field pattern corotates with the sun. At the orbit of the earth, the width of the sectors is of the order of 10^8km, and their azimuthal velocity is $\sim$400 km/sec. The convection of the sector structure spatial inhomogeneities past the moon then appear as temporal fluctuations of frequency

$$f = v_c/\lambda$$

where $v_c \sim 400$ km/sec is the convection speed and λ is the spatial wavelength. The phase difference between two points separated by a distance Δx is

$$\Delta\phi = 2\pi \; \Delta x/\lambda$$

At the frequencies of interest here (< 1/day), the spatial wavelengths are large (> 10^7km) compared with the diameter of the moon. Thus it is appropriate for our purposes to treat the field changes seen by the moon as being spatially uniform and temporally in phase.

The power density spectrum of the interplanetary magnetic field is shown in Figure 2.2. The solid curve is taken from Siscoe et al. (1968), and the dashed curve is from Coleman (1968). The dependence on frequency in the range shown is approximately $f^{-1.5}$. According to the analysis of Coleman, at frequencies above 2×10^{-5}Hz (0.5 day period) the spectrum is dominated by fluctuations perpendicular to the spiral field. Below this frequency the spectrum is the result of fluctuations parallel to the spiral field direction, e.g., the change in sign of the spiral field across sectors. This is the most energetic portion of the spectrum, and contains the fluctuations of primary interest in this paper.

2.2 Electrical Conductivity of the Moon

The response of the moon to magnetic field changes is dependent upon the electrical properties of the lunar interior. To provide motivation for our eventual choice of a model, we now present a brief review of current knowledge of the electrical conductivity of the moon.
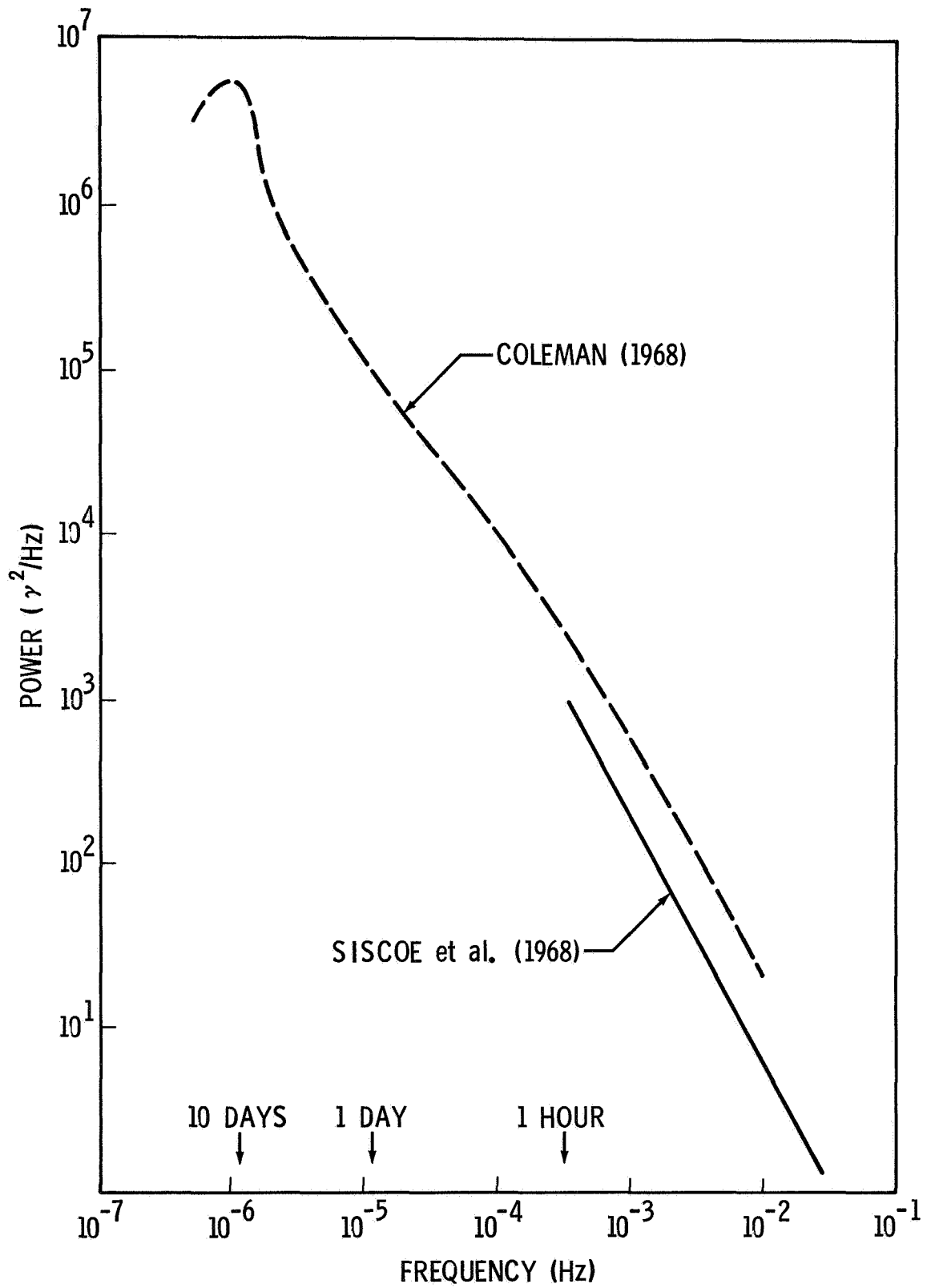
FIGURE 2.2 – POWER DENSITY SPECTRUM OF THE INTERPLANETARY
MAGNETIC FIELD

The lack of a disturbance in the solar wind on the sunlit side of the moon indicates that the lunar crust has a conductivity $\sigma < 10^{-5}$ $(\Omega\text{-m})^{-1}$. This upper bound is compatible with the surface being composed of either dry rocks, for which $\sigma < 10^{-7}$ $(\Omega\text{-m})^{-1}$, or rocks containing frozen water, for which $\sigma < 10^{-6}$ $(\Omega\text{-m})^{-1}$.

Present information on the conductivity of the lunar interior is based on theoretical studies. England et al. (1968) have calculated the electrical conductivity of the moon for various thermal models using the electrical properties of olivine. The two thermal models shown in Figure 2.3 are based on a young, 0.9 billion year, and an old, 4.5 billion year, chondritic moon.

The mineral composition of chondritic meteorites is predominately olivine (45%) and pyroxene (30%). There are at present no measurements of the electrical conductivity of chondrites. However, there is data on the electrical conductivity of olivine, including the effects of pressure. The conductivity of olivine is

$$\sigma = 55 \exp[-(.92 - 5.1 \times 10^{-3}P)/kT]$$

$$+ 4 \times 10^7 \exp[-(2.7 + 4.8 \times 10^{-3}P)/kT] \qquad (2.1)$$

where $P = 47[1-(r/b)^2]$ is the lunar pressure in kilobars, b is the radius of the moon, k is the Boltzmann constant, and T is the absolute temperature. The first term of (2.1) represents intrinsic semiconduction, and the second term is due to ionic conduction. At temperatures above about 1600°K, ionic conduction dominates.

The conductivity of the moon based on the two thermal models and the electrical properties of olivine is shown in Figure 2.4. For the young, cold moon, the maximum conductivity in the lunar interior is 10^{-2} $(\Omega\text{-m})^{-1}$, and for the old, hot moon it is almost $10(\Omega\text{-m})^{-1}$. The dashed curve represents a hot moon with partial melting in the interior. The partial melting results in an increase in the maximum conductivity to nearly $10^2(\Omega\text{-m})^{-1}$. There is a 3 to 4 order of magnitude
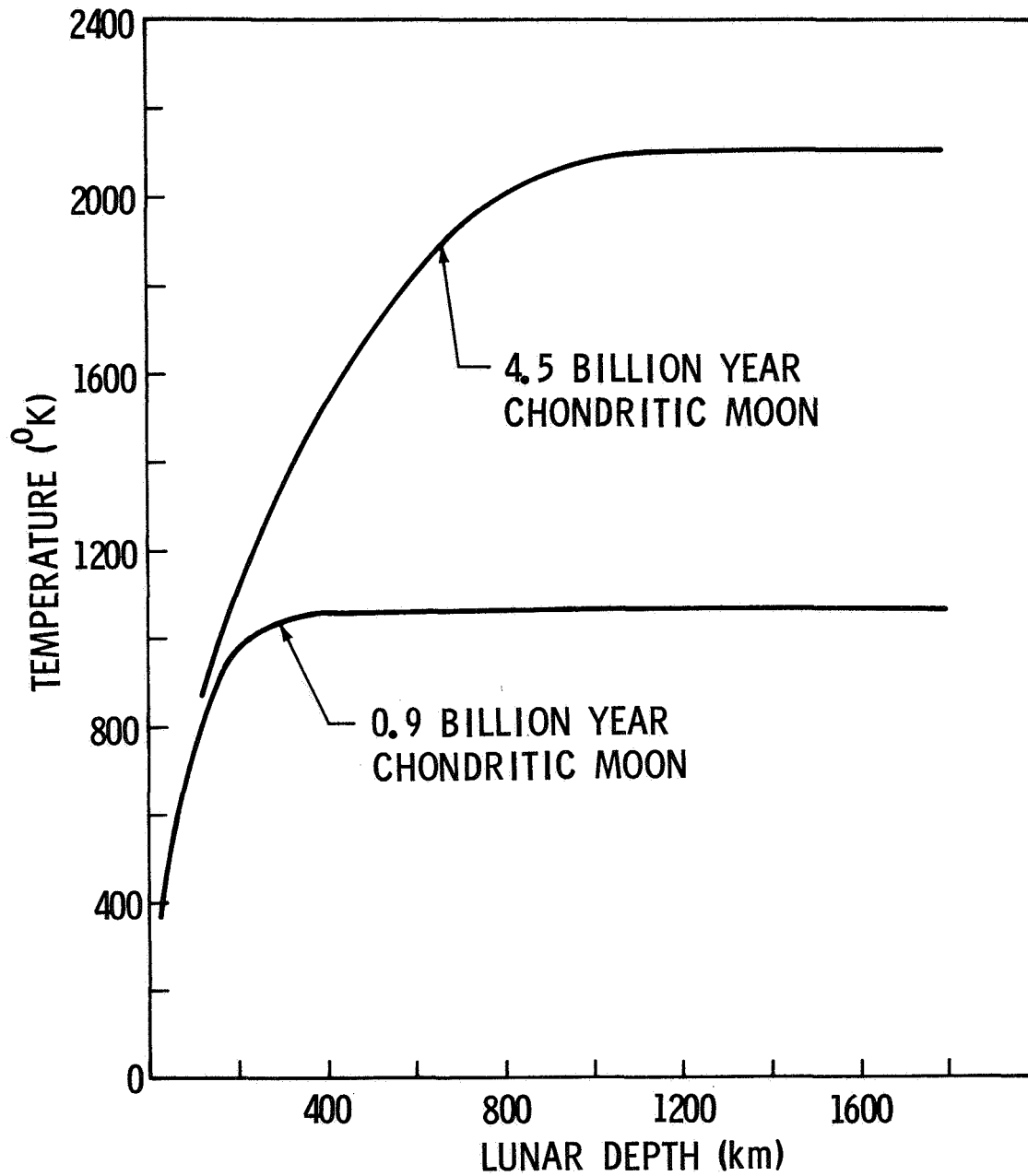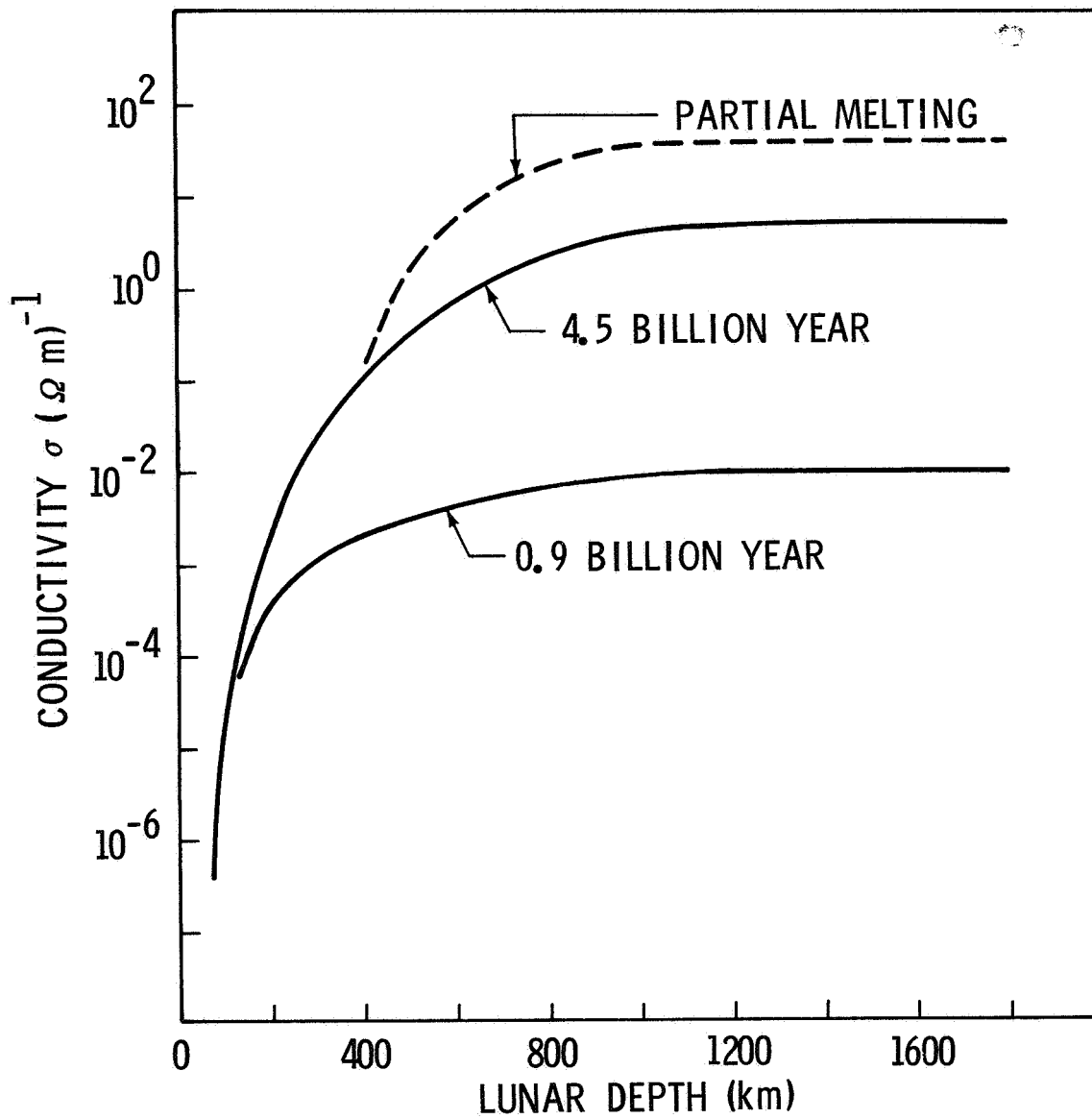
FIGURE 2.3 - LUNAR TEMPERATURE PROFILES

FIGURE 2.4 - LUNAR CONDUCTIVITY PROFILES

difference in the interior electrical conductivity between the cold and hot lunar models. Therefore even a crude measurement of the conductivity should allow one to distinguish between these proposed models of the lunar interior.

2.3 Models for Lunar Response

For all the models of the preceeding section, the conductivity increases rapidly in the first 300 km and is a relatively insensitive function of depth below 600 km. As an approximation we choose a simple two layer model, i.e., a uniform core of radius a and conductivity σ_1, surrounded by a uniform crust of thickness b-a and conductivity σ_2, with $\sigma_2 << \sigma_1$. This model retains the gross features of the conductivity profiles in Figure 2.4, and is mathematically convenient.

We wish to determine the response of this model to the spatially uniform time-varying magnetic field described in Section 2.1. The fluctuating field produces eddy currents in the lunar interior which give rise to an induced lunar magnetic field. The apparent absence of a disturbance in the solar wind on the sunlit side of the moon implies that the kinetic energy density of the solar wind there is greater than the energy density of any lunar magnetic fields. Consequently both induced and permanent lunar fields are compressed and excluded from the solar wind by currents which flow in the conductive plasma environment. The confining current is due to the deflection of solar wind particles by the induced magnetic field in a layer, above the sunlit lunar surface, whose thickness will be shown to be much smaller than the lunar radius. In this limit of large solar wind kinetic energy density, the volume current on the sunlit side of the moon may be approximated by a current sheet at the lunar surface. Only the unperturbed solar wind field exists exterior to the surface current. In Section 4 we show that this current sheet model is a systematic approximation to the actual confining solar wind currents on the sunlit side.

In the anti-solar direction there exists a plasma void due to the interception of solar wind particles at the lunar surface, and we anticipate the induced field to be substantially confined within the cavity region. Here the confinement is controlled by currents which flow at the boundaries between the undisturbed solar wind and the plasma cavity, and the situation is much more complex than on the sunlit side. We therefore restrict our attention to the study of the sunlit side and, for mathematical convenience, compute the sunlit side solution by replacing the confining solar wind currents, that

exist in the anti-solar direction, by a surface current on the back side of the moon, which is identical to that on the sunlit side. By introducing this approximation we sacrifice the ability to calculate corrections to the sunlit side solution which arise from the asymmetary between the solar and anti-solar directions. In Section 4 a qualitative picture of the effects of the interaction in the anti-solar direction is presented, and a quantitive estimate of the error introduced is given. The error is estimated by computing the contribution to the front side surface magnetic field due to the back side model surface current, which contribution is shown to be small.

3.0 RESPONSE TO TIME-VARYING FIELDS

The problem is most conveniently solved by performing a Fourier time analysis of the field. The procedure then reduces to computing the response of the moon to a uniform, time-varying component of the solar wind field, $\underline{B} = \underline{B}_o e^{-i\omega t}$. The formalism of the resulting vector boundary value problem is treated in the Appendix. The model admits only a poloidal magnetic field solution which is independent of the azimuthal angle ϕ. The geometry is shown in Figure 3.1. The solution in the lunar interior is (hereafter omitting the time dependence $e^{-i\omega t}$)

$$\underline{B} = \frac{1}{k} \nabla \times \nabla \times (\underline{r}\psi) \quad , \tag{3.1}$$

where

$$k^2 = i\mu\sigma\omega + \varepsilon\mu\omega^2 \simeq i\mu\sigma\omega \quad , \tag{3.2}$$

and ψ is the solution of the scalar Helmholtz equation,

$$\psi = \sum_{n=o}^{\infty} \psi_n = \sum_{n=o}^{\infty} [\alpha_n j_n(kr) + \beta_n y_n(kr)]P_n(\cos\theta) \tag{3.3}$$

Here $j_n(z)$ and $y_n(z)$ are the spherical Bessel functions, and $P_n(\cos\theta)$ the Legendre polynomials. The components of $\underline{B}$ are
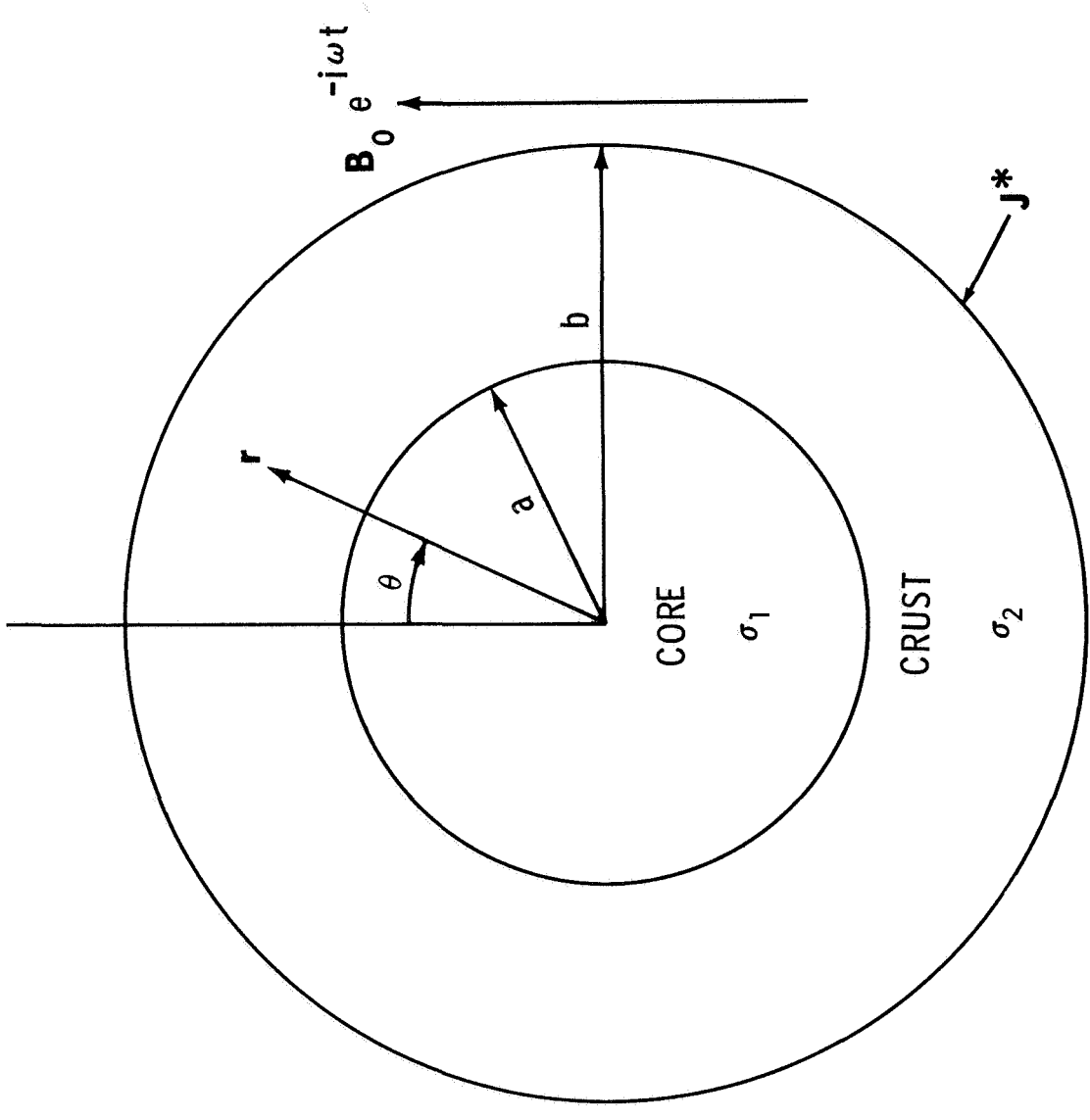
FIGURE 3.1 – GEOMETRY FOR RESPONSE OF THE MOON TO A HARMONIC
COMPONENT OF THE INTERPLANETARY MAGNETIC FIELD

$$B_r = \sum_{n=1}^{\infty} \frac{n(n+1)}{kr} \psi_n \quad , \tag{3.4}$$

$$B_\theta = \frac{1}{kr} \sum_{n=0}^{\infty} \frac{\partial^2}{\partial r \partial \theta} [r\psi_n] \tag{3.5}$$

A separate set of equations (3.3) - (3.5) exists for the core $(k = k_1)$ and the crust $(k = k_2)$. The coefficients α_n and β_n for the core and crust are determined from the following boundary conditions

$$r = o \; : \quad B_r, \; B_\theta < \infty \quad , \tag{3.6}$$

$$r = a \; : \quad B_r, \; B_\theta \text{ continuous} \; , \tag{3.7}$$

$$r = b \; : \quad B_r = B_o \cos\theta = B_o P_1(\cos\theta) \quad . \tag{3.8}$$

The surface current J_ϕ^* at $r = b$ is determined by the magnitude of the jump in B_θ required to reduce the crust field to the interplanetary value, $-B_o \sin\theta$. From the boundary condition at $r = b$, it is apparent that only the $n = 1$ term will survive in the sum (3.3).

The core and the crust solutions are characterized by the parameters $|kL|^2 = \omega\tau_c$. Since $\sigma_2 << \sigma_1$, $|k_2| << |k_1|$ and we need not consider the general case $|k_1 a| = O(|k_2 b|) = O(1)$. It suffices to consider the two limiting cases $|k_2 b|^2 \to 0$ with $|k_1 a|^2$ finite, and $|k_1 a|^2 \to \infty$ with $k_2 b$ finite. The former corresponds to a dielectric crust and may be viewed as the lowest order solution in a systematic expansion in powers of the small parameter $|k_2 b|^2$. For a crust conductivity of 10^{-5} $(\Omega\text{-m})^{-1}$, this approximation is valid for periods $T >> 4$ min. The second limiting case corresponds to a perfectly conductive core

and may be viewed as the lowest order solution in a systematic expansion in powers of the small parameter $|k_1a|^{-2}$. For a representative core conductivity of 1 $(\Omega\text{-m})^{-1}$ and a = 1.1 x 10^3km, this approximation is valid for periods T << 100 days. Thus for the above values of the parameters, the entire frequency spectrum is included in the two limits.

3.1　Dielectric Crust

In the limit $|k_2b|^2 \to 0$, $\underline{B} = \nabla\psi$ in the crust (Morse and Feshbach, 1953), where ψ is now the solution of Laplace's equation,

$$\psi = (\alpha r + \beta r^{-2})P_1(\cos\theta)　.　\tag{3.9}$$

Utilizing the boundary conditions (3.6) - (3.8), we obtain the following solutions for B_r and B_θ:

Core $0 \le r \le a$

$$B_r = 3B_o \frac{\lambda}{k_1 r} \frac{j_1(k_1 r)}{j_o(k_1 a)} \cos\theta \tag{3.10}$$

$$B_\theta = -\frac{3}{2} B_o \frac{\lambda}{j_o(k_1 a)} [j_o(k_1 r) - \frac{1}{k_1 r} j_1(k_1 r)]\sin\theta \tag{3.11}$$

Crust $a \le r \le b$

$$B_r = B_o\lambda[1 - R(\frac{a}{r})^3]\cos\theta \tag{3.12}$$

$$B_\theta = -B_o\lambda[1 + \frac{1}{2} R(\frac{a}{r})^3]\sin\theta \tag{3.13}$$

where

$$R = 1 - 3j_1(k_1 a)[k_1 a j_o(k_1 a)]^{-1} \tag{3.14}$$

$$\lambda = [1 - (\frac{a}{b})^3 R]^{-1}　.　\tag{3.15}$$

The surface current in the azimuthal direction at $r = b$ is

$$J^*_\phi = \frac{3}{2} \frac{B_o}{\mu} \lambda \left(\frac{a}{b}\right)^3 R \sin\theta \quad . \tag{3.16}$$

The crust solution (3.12) and (3.13) has a simple interpretation. If we look at the limit $b \to \infty$, the factor $\lambda \to 1$ and we recover the solution for a conductive sphere subjected to a uniform, time-varying vacuum magnetic field, i.e., the sum of a uniform field B_o and an induced dipole field of magnitude RB_o. We may therefore identify R as a complex reflection coefficient for the core. Expressed in terms of elementary functions, R assumes the form

$$R = \left[1 - \frac{3}{2x} \frac{\sinh 2x - \sin 2x}{\cosh 2x - \cos 2x}\right] - i \frac{3}{2x}\left[\frac{\sinh 2x + \sin 2x}{\cosh 2x - \cos 2x} - \frac{1}{x}\right] , \tag{3.17}$$

where $x = a/\delta_1$ and $\delta_1 = (2/\mu\sigma_1\omega)^{1/2}$ is the skin depth of the core. A plot of R as a function of a/δ_1 is presented in Figure 3.2. For a highly conductive core $x \gg 1$ and $R \to 1$, while in the opposite limit of a poorly conductive core $R \to 0$ as expected. The reflection coefficient is a sensitive function of the core parameters in the range $1 < a/\delta_1 < 10$. For a lunar core of conductivity $\sigma_1 = 1 \ (\Omega\text{-m})^{-1}$ and radius $a = 1.1 \times 10^3 \text{km}$, this corresponds to periods in the range between 0.5 and 55 days.

We identify the crust solution as the sum of a uniform and a dipole field, increased by the factor λ. From (3.15) we see that λ represents a volume compression of the field, which manifests the confinement of the field by the solar wind. For a perfectly conductive core and a crust of 600 km thickness, we obtain $\lambda = 1.4$.

Figure 3.3 shows the magnitude of the field components as a function of radial distance and core skin depth. When the skin depth is equal to the conductive core radius, the field components B_r and B_θ are essentially uniform throughout the core and crust. As the skin depth decreases, the radial component
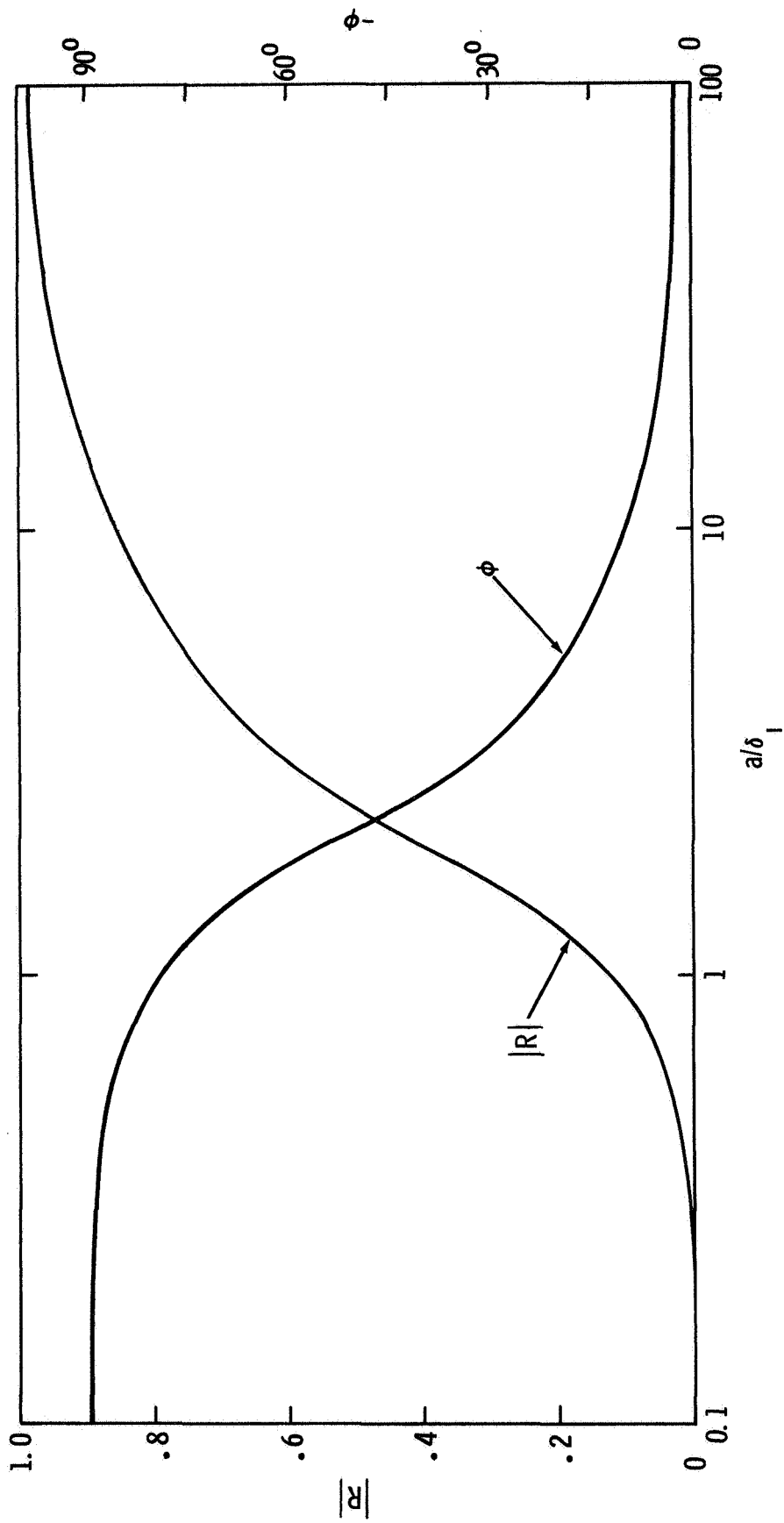
FIGURE 3.2 - MAGNITUDE $|R|$ AND PHASE ϕ OF THE REFLECTION COEFFICIENT $R = |R| \ e^{i\phi}$ AS A FUNCTION OF CORE SKIN DEPTH δ_1

B_r is diminished within the core and crust. Similarly, B_θ decreases with decreasing skin depth near the center of the core, but it rises to values greater than the source field near the core surface and in the crust. The compression of the field arising from solar wind currents is evidenced by comparing the solution with that which would exist in the absence of the confining solar wind currents (see unconfined field solution in Figure 3.3).

3.2 Perfectly Conductive Core

The lunar core behaves like a perfect conductor when $|k_1 a|^2 \gg 1$. For a core conductivity of $1(\Omega\text{-m})^{-1}$ this occurs for periods $T \ll 100$ days. Since ψ is a solution of the Helmholtz equation, $|k_1 a|^2 \to \infty$ forces $\psi \to 0$. Consequently the magnetic field is excluded from the core, and $B_r = B_\theta = 0$ for $r < a$. To determine the field in the crust, the boundary conditions (3.7) at $r = a$ must be relaxed to permit a surface current. At $r = a$ we may only require $B_r = 0$. Then (3.3) – (3.5) with the boundary condition (3.8) yield the following solution in the lunar crust:

$$B_r = \eta \, B_o \, \frac{b}{r}\Big[y_1(k_2 a)j_1(k_2 r) - j_1(k_2 a)y_1(k_2 r)\Big]\cos\theta \quad , \quad (3.18)$$

$$B_\theta = -\frac{1}{2} \, \eta \, B_o \, \frac{b}{r}\Big\{y_1(k_2 a)[k_2 r j_0(k_2 r) - j_1(k_2 r)]$$

$$- j_1(k_2 a)[k_2 r y_0(k_2 r) - y_1(k_2 r)]\Big\}\sin\theta \quad , \quad (3.19)$$

where $\eta = [y_1(k_2 a)j_1(k_2 b) - j_1(k_2 a)y_1(k_2 b)]^{-1}$.

The forms of (3.18) and (3.19) are not very transparent and are indicative of the algebraic complexities one encounters in proceeding to multi-layered lunar models. The field components are shown in Figure 3.4 where the parametric dependence on the crust skin depth is illustrated. At large values of the skin depth the induced field results primarily from the currents at the surface of the perfectly conductive core. In fact, in the limit $|k_2 b| = \sqrt{2}b/\delta_2 \ll 1$ we obtain
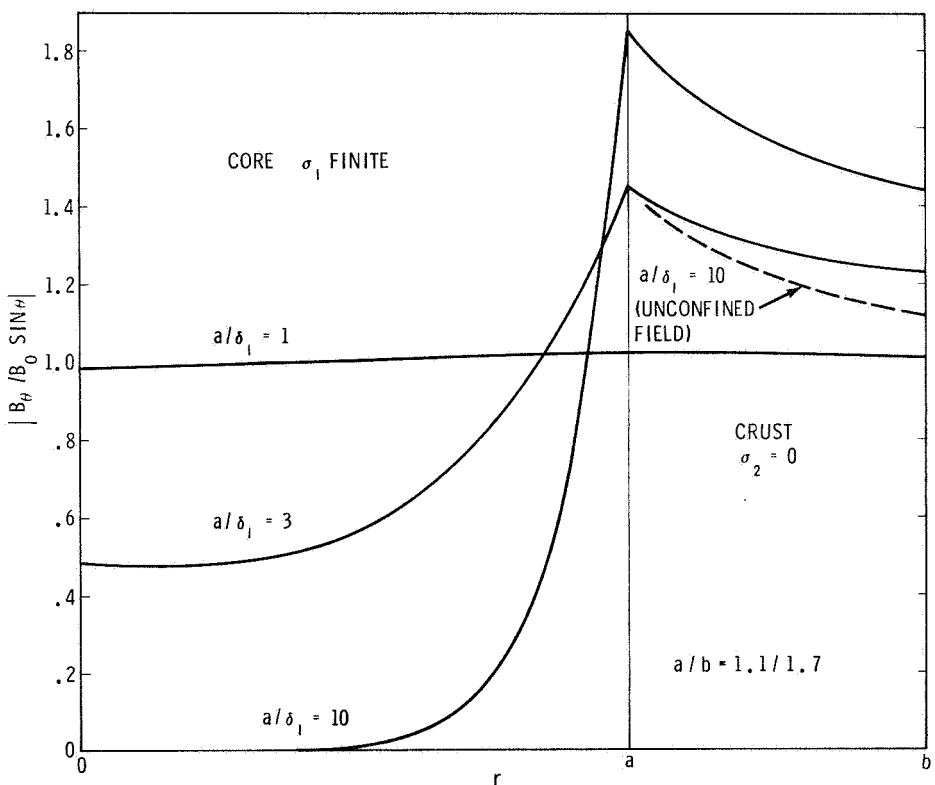
CORE σ_1 FINITE

CRUST $\sigma_2 = 0$

$|B_r/B_0 \cos \theta|$

1.2

1.0

.8

.6

.4

.2

0

$a/\delta_1 = 1$

$a/\delta_1 = 3$

$a/\delta_1 = 10$ (UNCONFINED FIELD)

$a/\delta_1 = 10$

0   a   b

r

CORE σ_1 FINITE

$|B_\theta/B_0 \sin \theta|$

1.8

1.6

1.4

1.2

1.0

.8

.6

.4

.2

0

$a/\delta_1 = 1$

$a/\delta_1 = 3$

$a/\delta_1 = 10$ (UNCONFINED FIELD)

$a/\delta_1 = 10$
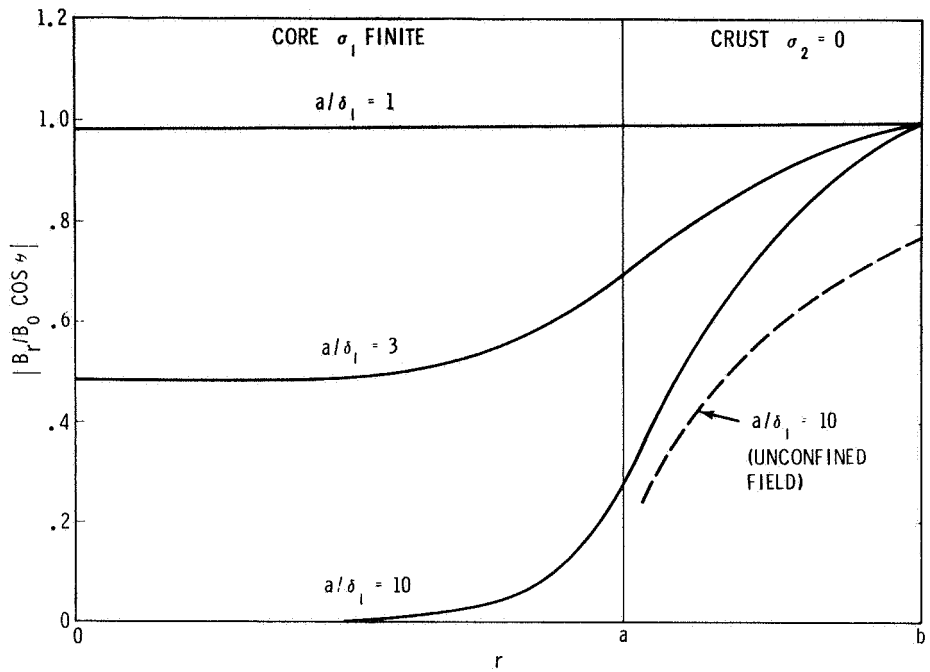
CRUST $\sigma_2 = 0$

$a/b = 1.1/1.7$

0   a   b

r

FIGURE 3.3 - MAGNITUDES OF B_r AND B_θ AS A FUNCTION OF RADIUS AND
CORE SKIN DEPTH, $\delta_1 = (2/\mu\sigma_1\omega)^{1/2}$, FOR THE CASE OF A
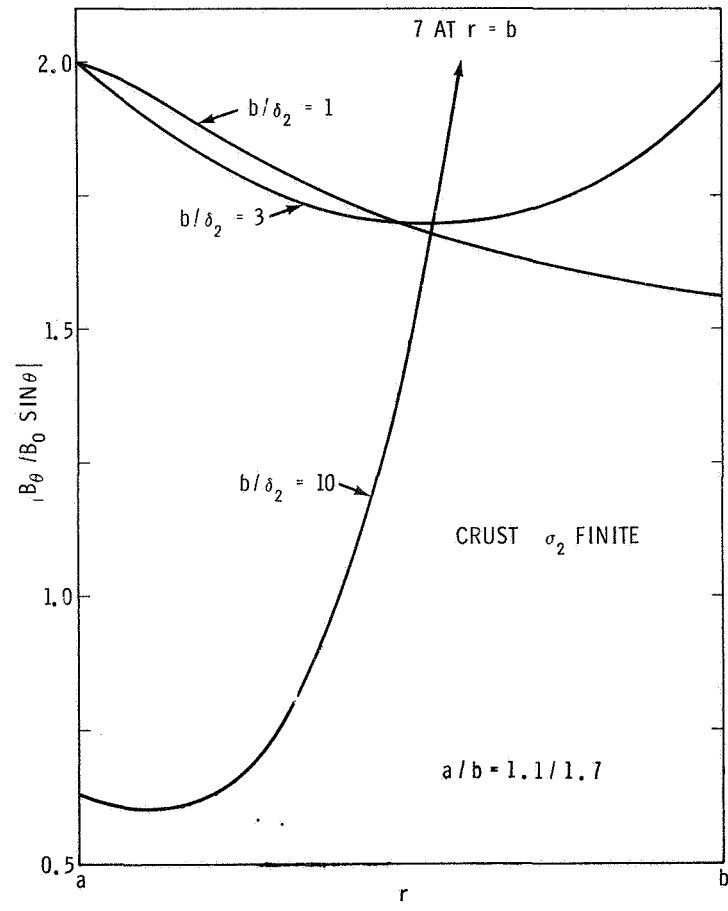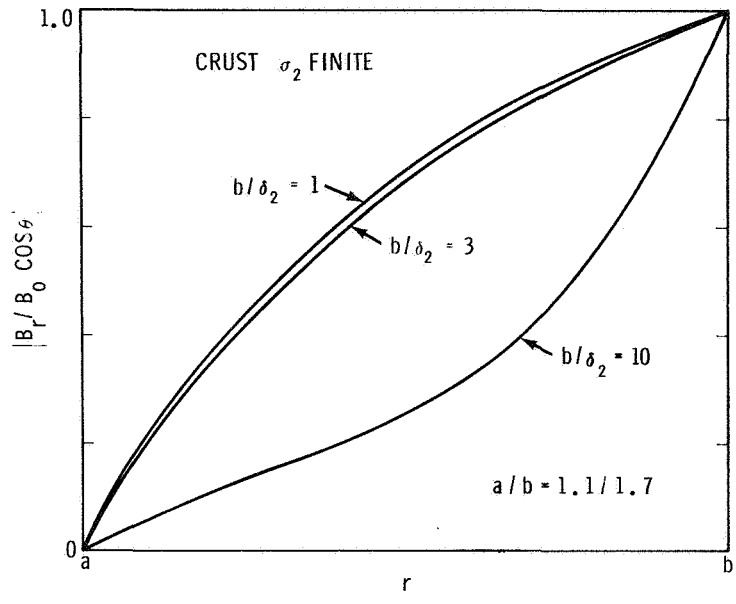DIELECTRIC CRUST AT A FIXED VALUE OF a/b

FIGURE 3.4 - MAGNITUDES OF B_r AND B_θ IN THE CRUST AS A FUNCTION OF RADIUS AND CRUST SKIN DEPTH, $\delta_2 = \sqrt{2}/|K_2| = (2/\mu\sigma_2\omega)^{1/2}$, FOR THE CASE OF A PERFECTLY CONDUCTIVE CORE AT A FIXED VALUE OF a/b

$$B_r = B_o[1 - (a/r)^3][1 - (a/b)^3]^{-1}\cos\theta[1 + 0(|k_2 b|^2)] \ .$$

This, as well as the corresponding form for B_θ, matches with the dielectric crust solution expanded for $|k_1 a| >> 1$. As the crust skin depth decreases, the field is diminished deep within the crust, while the near surface values of B_θ increase rapidly. When $b/\delta_2 \geq 3$, the induction due to current flow in the crust is appreciable. For a crust conductivity $\sigma_2 = 10^{-5}$ $(\Omega\text{-m})^{-1}$, this condition is satisfied at frequencies greater than 0.1 Hz.

4.0 DISCUSSION OF THE MODEL

First, a plausibility argument for the use of the surface current model on the sunlit side of the moon is presented which indicates that this model is a systematic approximation to the true current distribution. A surface current model may be viewed as a mathematical limiting process,

$$J_\phi^* = \lim_{\Delta \to 0} \Delta \ J_\phi$$

where the limit is taken at fixed confining current. Here J_ϕ is the confining current density, and Δ is the thickness of a layer, adjacent to the sunlit lunar surface, where the confining solar wind currents flow, and where B_θ decreases from its lunar surface value to that of the undisturbed solar wind. A necessary condition for the use of the surface current approximation is $\Delta << (b-a)$, i.e., Δ must be shorter than the smallest relevant length scale in our model. It is also required that Δ be small compared with the solar wind proton Larmor radius based on the streaming proton velocity. Satisfying this condition ensures that the proton orbits experience a negligible perturbation, as required for compatibility with the observed absence of an interaction of the solar wind with the moon on the sunlit side.

An upper bound for Δ can be estimated without resorting to a detailed calculation of the physical mechanism which produces the confining current. Since it is by virtue of the large proton energy that the lunar magnetic field is compressed, the protons must be central to the confinement process. An upper bound for Δ is obtained by assuming all the current to be carried by the protons. Then as the protons traverse the distance Δ, their trajectories are perturbed by the magnetic field gradient. This produces an ordered change in the proton velocity of order of magnitude $(\Delta/r_B)V$, where V is the proton streaming velocity, and $r_B = MV/eB_o$ is the proton Larmor radius based on V. For typical solar wind parameters $r_B \sim 500$ km. The current density which results from this velocity change is

$$ J_\phi \sim ne \, \frac{\Delta}{r_B} \, V $$

where n is the proton number density. The upper bound for Δ is obtained from the relation $J_\phi^* \sim \Delta J_\phi$, where J_ϕ^* is given by (3.16). We therefore estimate

$$ \Delta \sim \left(\frac{B_o^2/2\mu}{MnV^2} \right)^{1/2} r_B << r_B \quad . $$

The quantity in brackets is the ratio of the magnetic field energy density to the proton energy density, and is much less than 1. Thus, in a layer whose thickness is small compared with r_B and (b-a), the solar wind protons can provide a large enough current to confine the induced lunar magnetic field. The presence of the more mobile solar wind electrons can serve only to decrease the value of Δ. Thus, the actual confining current distribution exists in a layer of thickness $<< r_B$, and our surface current model on the sunlit side of the moon is a systematic approximation, correct in the asymptotic limit $\Delta/a \rightarrow 0$.

We now consider qualitatively the corrections to our solution arising from the asymmetry between the solar and antisolar directions. To facilitate the discussion we assume that

the moon has a dielectric crust. The crust solution is then
the sum of a uniform and an aligned dipole field, modified by
the presence of currents which flow in the solar wind. There-
fore the field confining currents must exist adjacent to the
lunar surface on the sunlit side, and in the region between
the undisturbed solar wind and the plasma void in the anti-
solar direction. The latter neglects the possibility of plasma
existing in the void region and producing a significant current.
The resulting induced field configuration is shown schematically
in Figure 4.1. The induced field in the anti-solar direction is
similar to that of a skewed dipole confined within a cylinder.

On the anti-solar side of the moon we have replaced
the true current distribution by the same surface current sheet
J_ϕ^* used on the sunlit side in order to preserve the symmetry in
our model. To obtain a quantitative estimate of the error in-
troduced by this model for the back side currents, we have
numerically computed the contribution to the magnetic field at
a point on the surface of the sunlit hemisphere arising from
the model back side surface current given by (3.16), assuming a
perfectly conductive core of radius 1.1×10^3km. The solution
is quantitatively correct in regions where this contribution
is small. This criterion is proper, because the model surface
current on the back side of the moon makes a larger contribu-
tion to the sunlit side field than the actual current distri-
bution which produces less confinement in the anti-solar
direction. At the subsolar point, the contribution to the
magnetic field arising from the back side surface current is
computed to be 5%. The contribution rises to 12% at a sunlit
side surface point in the ecliptic plane which is $\pi/4$ from the
subsolar point. Hence we estimate that the error introduced
by our surface current model is small in the vicinity of the
subsolar point, and increases as one approaches the limb. The
determination of the actual error would require the comparison
of our solution with that obtained for the asymmetrical prob-
lem.

5.0 APPLICATION TO THE ALSEP MAGNETOMETER EXPERIMENT

5.1 Magnetic Environment of the Moon

Figure 5.1 shows the moon in its orbit about the
earth, together with the positions of the earth's bow shock,
the transition region and the geomagnetic tail. Upstream from
the shock the interplanetary field lies, on the average, in
the ecliptic plane and makes a spiral angle of approximately
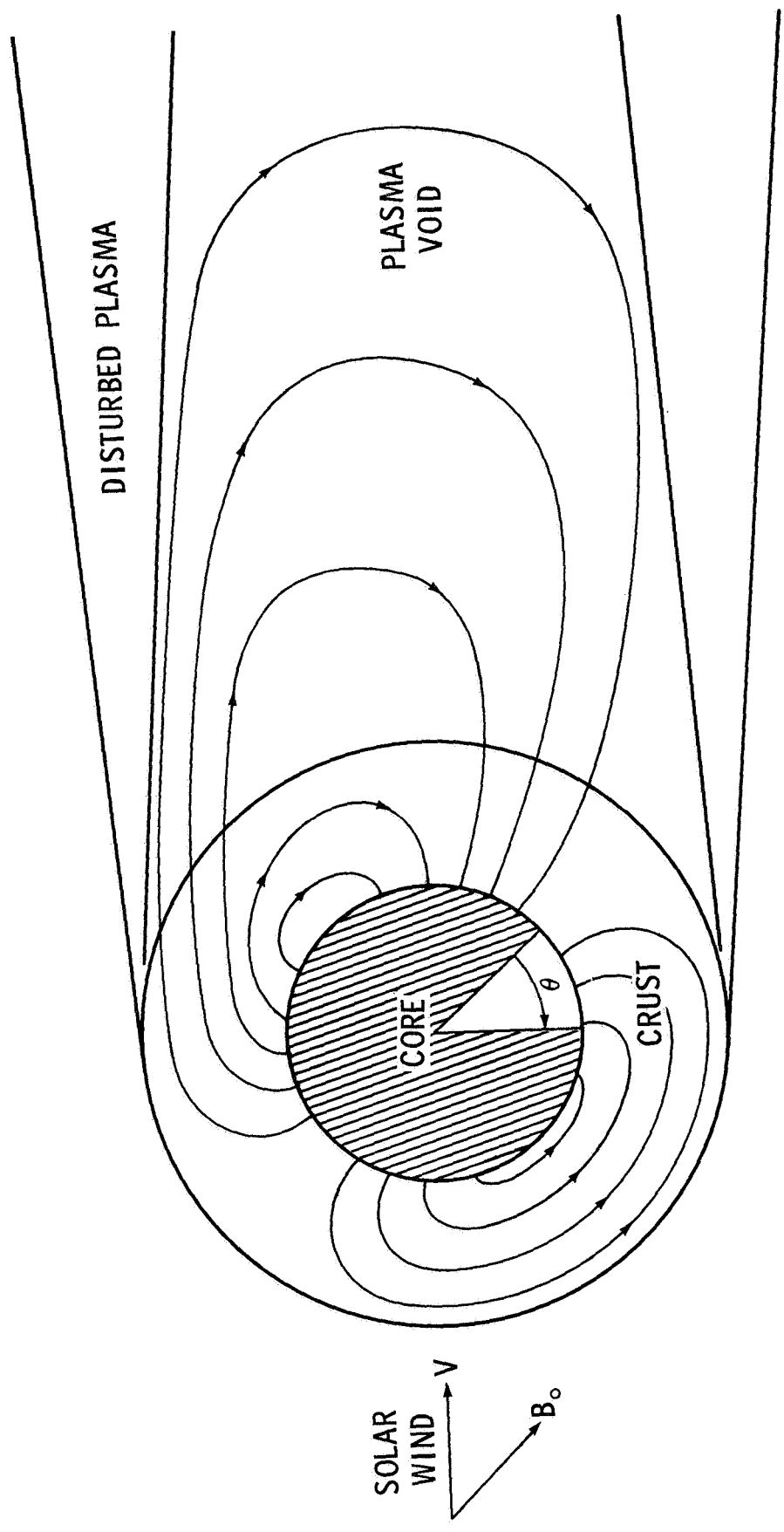45° with the vector to the sun. At the orbit of the moon there

FIGURE 4.1 - SCHEMATIC ILLUSTRATION OF THE CONFINEMENT BY THE SOLAR WIND OF A HARMONIC COMPONENT OF THE INDUCED LUNAR MAGNETIC FIELD
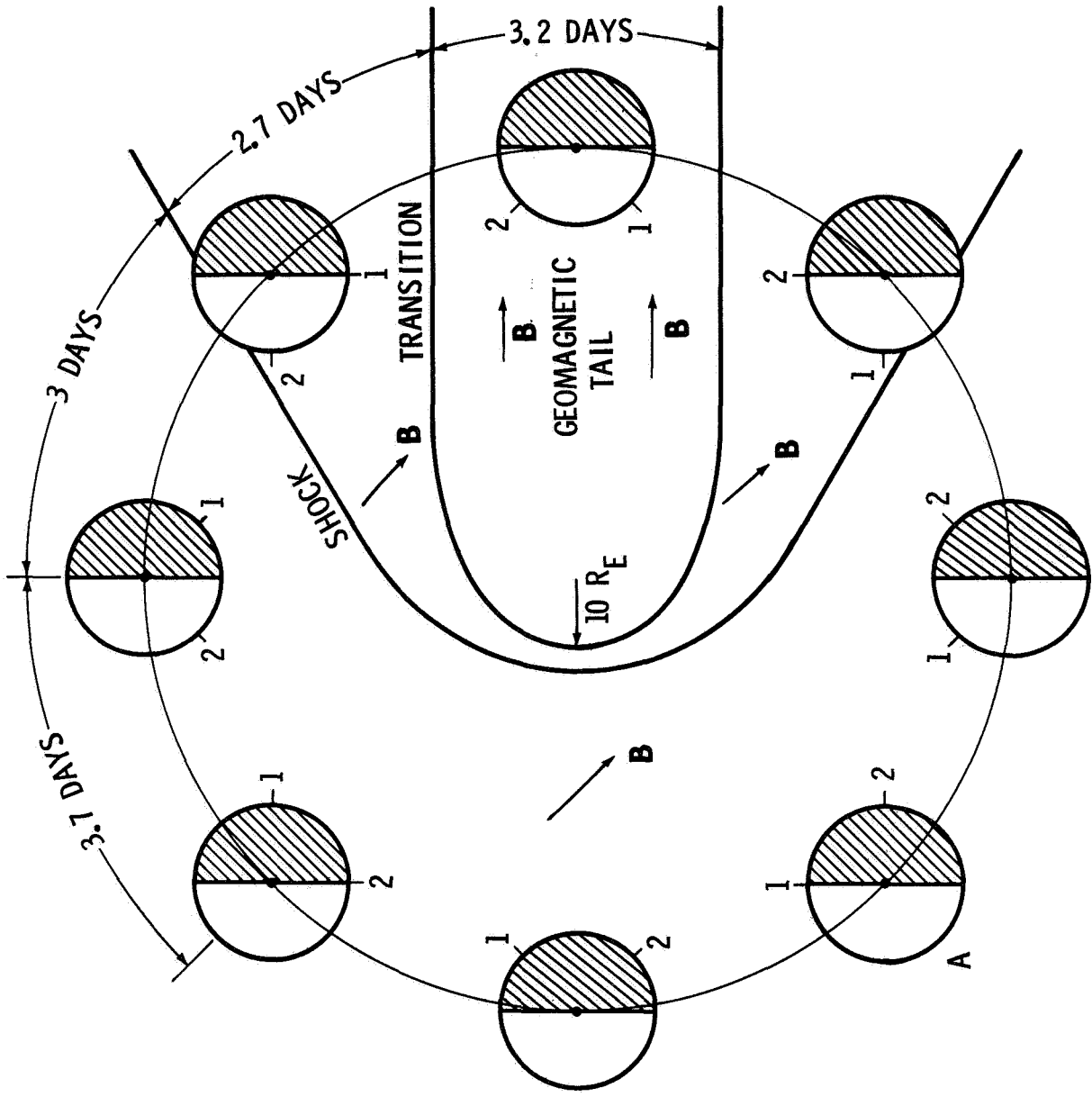
FIGURE 5.1 - ORBIT OF THE MOON, SHOWING BOW SHOCK AND GEOMAGNETIC TAIL

is a small change in the spiral angle through the shock, accompanied by a jump in the magnitude of the field (Behannon, 1968). The interplanetary field, including the sector structure, is convected across the shock with these changes (Fairfield and Ness, 1967). The presence of the magnetosphere causes a realignment of the interplanetary magnetic field in the transition region. In the vicinity of the geomagnetic tail boundary, the field tends to be aligned tangent to the boundary, and this realignment produces a large component of the field out of the ecliptic plane. Observations in the transition region at lunar orbital distances show the field direction deviating by as much as ±60° out of the ecliptic (Behannon, 1968). These fluctuations out of the ecliptic have a time scale of several hours and have been taken to indicate that the interplanetary lines of force are alternately draped over and under the magnetosphere and the geomagnetic tail.

When the moon is in the transition region, the kinetic energy of the solar wind plasma is large enough to confine any induced lunar magnetic fields. Consequently our model is applicable in the transition region as well as in the undisturbed solar wind. Although the interplanetary magnetic field in the transition region has large fluctuations out of the ecliptic plane, these fluctuations have periods which are much less than those associated with the sector structure.

In the geomagnetic tail, the magnitude of the field is larger than in the transition region, and the field vector points either toward or away from the sun, depending on whether the moon is above or below the neutral sheet. Thus, as the moon traverses the geomagnetic tail, it experiences a time-varying magnetic field with a period on the order of days. Confinement of the induced field should occur if the energy density of the induced field is less than the energy density of the geomagnetic plasma environment. Since the induced field and geomagnetic plasma energy densities can be of the same order of magnitude, it is not known at present whether confinement occurs.

The fact that Explorer 35, while orbiting the moon in the geomagnetic tail, did not detect any significant magnetic variations attributable to the moon, establishes an upper limit of a few gammas for any lunar fields at an altitude of 800 km (Ness et al.,1967). Thus the lack of observable lunar fields at this altitude can be taken to indicate either that the induced field is confined, or that it is unconfined and less than a few gammas in strength. The latter alternative does not indicate that the moon is a poor conductor, as an induced field

of 1γ at 800 km, assuming an unconfined induced dipole, would result from a perfectly conductive core of radius 1.1×10^3 km in a typical geomagnetic tail source field of 8γ.

5.2 ALSEP Magnetometer Site Selection

To interpret the lunar surface magnetic data by application of the theory developed in this paper, the criterion for selection of an ALSEP magnetometer site is that the continuous observing time spent on the sunlit lunar hemisphere, while the moon is outside the geomagnetic tail, should be maximized. The magnetometer location is restricted to proposed Apollo landing sites, which lie near the lunar equator and within about 45° from the subearth point. From Figure 5.1, it is readily seen that, of the proposed Apollo landing sites, the one furthest from the subearth point represents the most desirable magnetometer location.

Consider, for example, a magnetometer at site 1, 45° from the subearth point in Figure 5.1. As the moon progresses in its orbit, starting from position A, the magnetometer at 1 spends approximately 6.7 days in the undisturbed solar wind, during which time it moves from the terminator to within 8° of the subsolar point. For the next 2.7 days the moon is in the transition region and the observation site is near the subsolar point. During the major portion of the remaining part of the orbit, the magnetometer at site 1 is either in the geomagnetic tail or on the dark hemisphere. Thus for site 1, there are about 9 days during which continuous data may be collected while the magnetometer is on the sunlit hemisphere and in the solar wind. For comparison, a magnetometer located at the subearth point provides only 6 days of continuous data during which the conditions required for the theory exist.

It has been suggested that the recently discovered mass concentrations in the ringed marias may be due to large masses of meteoric iron (Muller and Sjogren, 1968). The gravimetric map of the nearside lunar hemisphere, including the location of the Apollo landing sites, is shown in Figure 5.2. The largest acceleration is observed over Mare Imbrium, and is equivalent to an acceleration that would be produced by a spherical iron mass of 50 km radius at a depth of 50 km. A mass of this size with the electrical conductivity of iron, $\sigma \sim 10^5 (\Omega\text{-m})^{-1}$, would produce a substantial induced field. If this is the case, the magnetometer must be located sufficiently
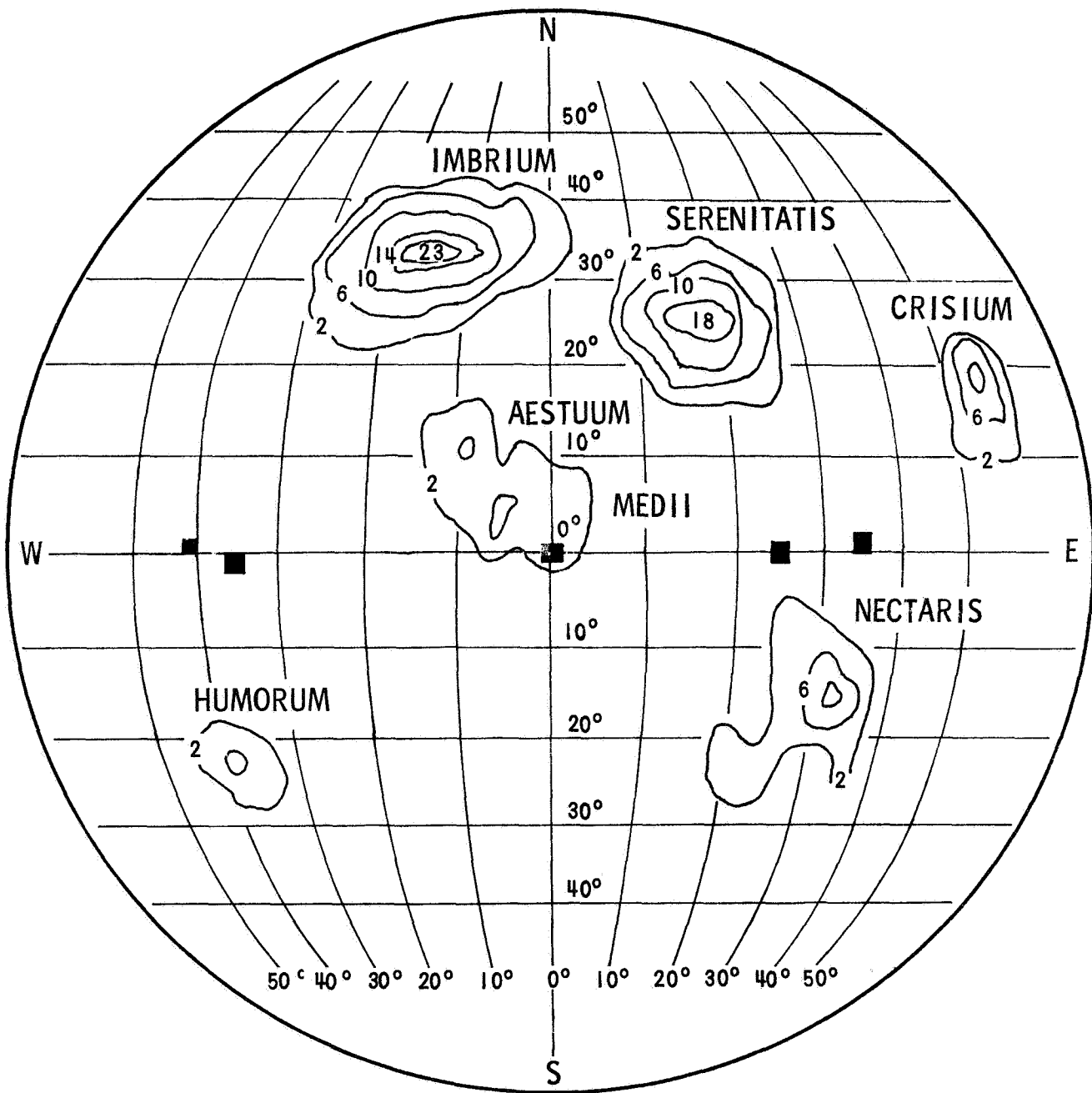
FIGURE 5.2 - LUNAR GRAVIMETRIC MAP, CONTOUR INTERVAL 4 MM/SEC^2. APOLLO LANDING SITES SHOWN BY BLACK SQUARES.

far from any mass concentration so that the magnetic field induced in the core dominates the field induced by the mass. The
induced field of such a meteoric iron mass has a dipole-like
character at distances large compared with its linear dimension.
Therefore the induced field will fall below the resolution of
the magnetometer ($\sim 0.1\gamma$) if the magnetometer is located at a
distance comparable or greater than 4 times the characteristic
dimension of the disturbing mass. The separation between the
magnetometer and the suspected iron masses should then be of the
order of a few hundred kilometers. The eastern and western
Apollo landing sites are over 200 km from the closest mass concentrations at Mare Nectaris and Mare Humorum, respectively.
However, the central site is within 75 km of the small mass concentration near Sinus Medii. Thus, to minimize the effect of
possible induced fields, the preferential listing of the Apollo
sites is western, eastern, and central.

5.3   Interpretation of Lunar Surface Magnetic Data

We have proposed a model which enables us to calculate
the magnetic field induced in the moon by interplanetary magnetic field variations. The induced magnetic field at the lunar
surface is a function of the electrical conductivity $\sigma(r)$ in the
lunar interior. It is therefore of interest to investigate how
the ALSEP lunar surface magnetic field measurements, in conjunction with our theory, may be employed to determine this conductivity, and hence to provide information on the temperature of
the lunar interior.

The cold moon model has a maximum temperature of
$1200°K$, a core conductivity $\sigma \sim 10^{-2}$ $(\Omega\text{-m})^{-1}$, and therefore
a Cowling time $\tau_c \sim 0.15$ days. The hot moon models have maximum temperatures $> 2000°K$, core conductivities $1 < \sigma < 10^2$
$(\Omega\text{-m})^{-1}$, and Cowling times $15 < \tau_c < 1500$ days, with the higher
values arising from partial melting in the lunar interior. The
portion of the interplanetary magnetic field power spectrum
associated with field reversals has appreciable energy in the
period range from a few to tens of days. Thus the condition
$T \sim \tau_c$ can be satisfied for a range of possible core conductivities, and certainly for $\sigma \lesssim 1$ $(\Omega\text{-m})^{-1}$. Provided this condition is attained, the bulk of the moon surrounding the core will
appear to be poorly conductive. At such a frequency our core-
crust model with a dielectric crust is a reasonable representation for the electrical response of the moon. The core conductivity may then be calculated from lunar surface magnetometer
data. At the lunar surface (3.12) and (3.13) reduce to

$$B_r(\omega) = B_o(\omega)\cos\theta \quad , \tag{5.1}$$

$$B_\theta(\omega) = -H(\omega)B_o(\omega)\sin\theta \quad , \tag{5.2}$$

where

$$H(\omega) = [1 + \frac{1}{2}(\frac{a}{b})^3 R(\omega)][1 - (a/b)^3 R(\omega)]^{-1} \tag{5.3}$$

is the transfer function for our model of the moon and is shown in Figure 5.3. With B_o and θ established from independent observations of the interplanetary magnetic field, (5.1) may be used as a check on the accuracy of our model, and (5.2) can be solved for $H(\omega)$, which contains the two parameters a/b and $R(\omega)$ that characterize the electrical properties of the lunar core. Assuming the theory to be correct, the core conductivity can be estimated by a best parametric fit of (5.3) to the data. The independent measurement of the interplanetary magnetic field can be provided by either lunar or earth orbiting spacecraft. In the latter case the source spectrum at the moon is determined by assuming the field corotates, and applying the appropriate time lag or lead. Lacking an independent measurement of the interplanetary magnetic field, (5.1) can be used to determine the source spectrum if the angle θ is known. As was pointed out in Section 2.1, the fluctuations of period $T > .5$ days are predominantly parallel to the spiral field direction, so to a first approximation one may equate θ to the angle between the theoretical spiral direction and the radius to the observation point.

The above discussion of the interpretation of the data neglects certain effects caused by the rotation of the surface observation site with the moon. These effects are similar to those encountered in making magnetic field measurements from rotating satellites, and are discussed by Sonett (1966). The essence of the matter lies in the fact that the rotation of the observation point produces an amplitude modulation of the magnetic field. This is evident from the crust solution, (5.1) and (5.2), if we ascribe the effect of the rotation as producing the time dependence in the angle θ, $\theta = \Omega t$, where Ω is the angular rotation frequency of the moon. Alternatively, we can view this effect as resulting from the rotation of the source field at a frequency Ω measured with respect to a coordinate system fixed with the moon.
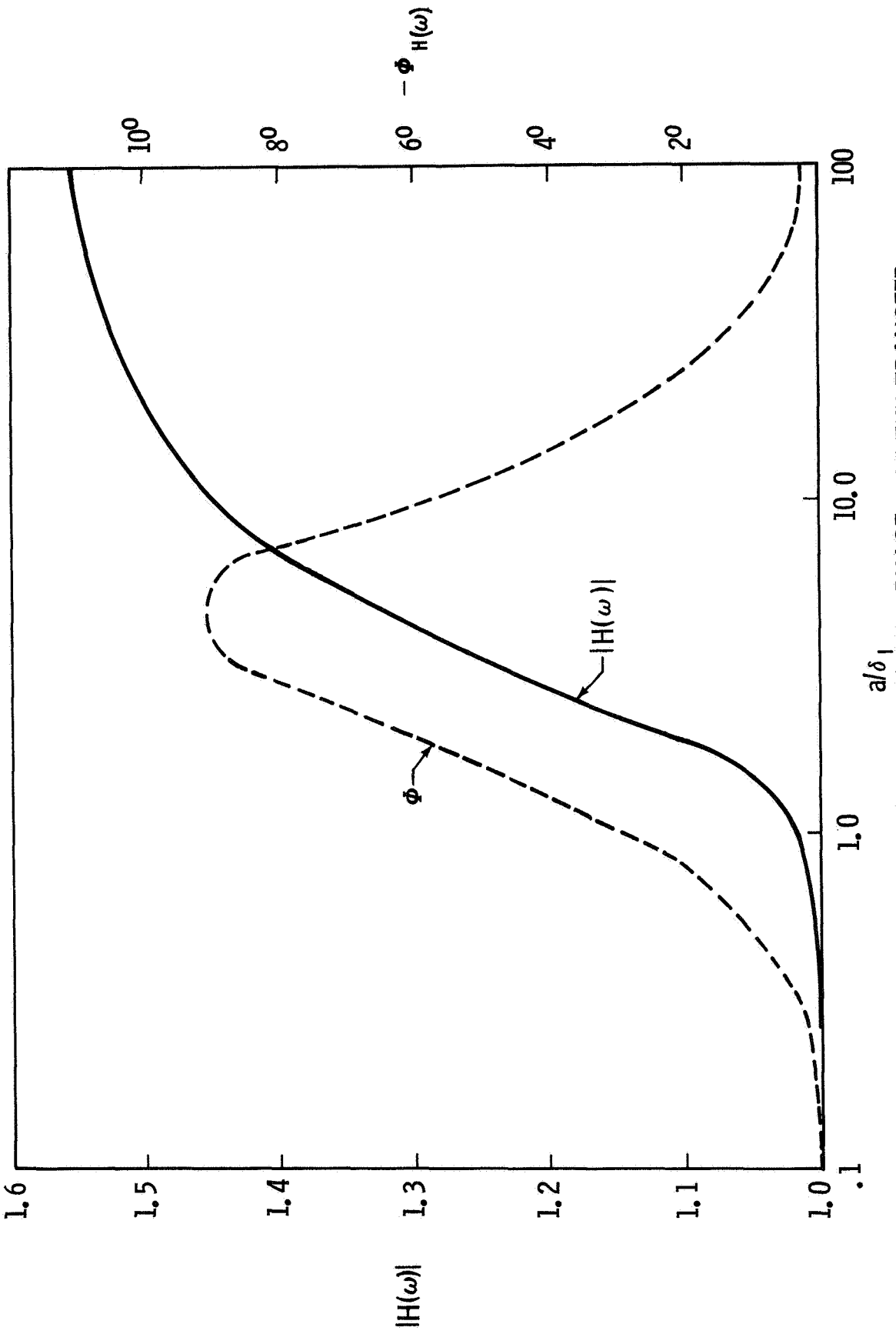
FIGURE 5.3 - MAGNITUDE $|H(\omega)|$ AND PHASE ϕ OF THE TRANSFER
FUNCTION FOR THE RATIO $a/b = 1.1/1.7$

The modulation of the fluctuations in the time domain is equivalent to the convolution of the source spectrum $B_o(\omega)$ with the spectrum of the rotation $M(\omega)$. The transfer function $H(\omega)$ is then determined by dividing the measured spectrum by the convolution of the source and rotational spectra. If our solutions (5.1) and (5.2) were exact over the entire lunar surface, then this simple sinusoidal amplitude modulation would give rise to a modulation spectrum $M(\omega)$ which consists of a pair of delta functions at $\omega = \pm\Omega$. Actually, the day-night asymmetry of the induced magnetic field configuration will produce a more complicated modulation spectrum containing harmonics of Ω.
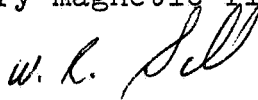
At frequencies much greater than Ω, the angular changes are small during the period of the fluctuation and the effects of rotation can be ignored. As the frequency of the fluctuations approaches Ω, the effects of the rotational modulation become important. Consider, for example, the data collected at site 1 of Figure 5.1 during the 9 day period when the magnetometer is on the sunlit hemisphere and in the solar wind. The effects of the lunar rotation may be approximated by a simple, sinusoidal modulation for periods of the order of a day, and ignored at much higher frequencies. Thus the observed time domain data can be transformed into the frequency domain, and $H(\omega)$ can be calculated for periods less than a few days. This approach should be adequate, as fluctuations with periods $T < 3$ days can be used to determine the core conductivity if $\sigma < 5 \ (\Omega\text{-m})^{-1}$. This range of conductivity encompasses the cold and hot (without partial melting) lunar models of England et al. If $\sigma > 5 \ (\Omega\text{-m})^{-1}$ only a lower bound may be placed on the conductivity for measurements made at periods $T < 3$ days. To determine higher values for the conductivity, the interpretation of the measurements must be extended to longer periods. As noted above, this requires a determination of the rotational modulation spectrum, including the effects of day-night asymmetry.

6.0 CONCLUSIONS
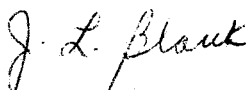
The fact that the spectrum of the interplanetary magnetic field has appreciable power at periods within the range of Cowling times for proposed lunar models suggests that there will be an observable lunar response. Interpretation of the response permits the calculation of the electrical conductivity of the moon. This provides information on the temperature of the lunar interior, which is central to theories of lunar formation and history.

The induced lunar fields are confined by the energetic solar wind, and hence measurements must be made on the surface. Confinement of the lunar field is also possible when the moon is in the geomagnetic tail. On the basis of the theory developed in this paper, if only one ALSEP magnetometer is to be deployed, it should be located as far from the subearth point as is compatible with the Apollo constraints. During each lunation, a magnetometer site 45° from the subearth point will provide continuous data for about 9 days when the moon is in the solar wind. Using our model, this length of continuous data can be used to measure the lunar response to interplanetary magnetic field variations with periods less than a few days. This is adequate to calculate the electrical conductivity of a lunar core if the conductivity is $\lesssim 5 \ (\Omega\text{-m})^{-1}$. This range is sufficient to distinguish between proposed hot and cold lunar models. If the Cowling time of the lunar core is substantially greater than a few days, only a lower bound on the conductivity can be obtained, unless the problems associated with data interpretation of very low frequency fluctuations are resolved.

An independent, simultaneous measurement of the interplanetary magnetic field spectrum is desirable as it provides a check on the accuracy of our model. Such measurements can be obtained by either a lunar orbiter or a spacecraft in the earth-moon vicinity. Lacking an independent measurement, the spectrum may be derived from measurements of the radial component of the field at the lunar surface, under the assumption that the fluctuations at the frequencies of interest are in the direction of the theoretical interplanetary magnetic field spiral angle.

W. R. Sill

J. L. Blank

1014-$\frac{\text{WRS}}{\text{JLB}}$-jan

BELLCOMM, INC.

REFERENCES

Behannon, K. W., Mapping of Earth's Bow Shock and Magnetic Tail
by Explorer 35, J. Geophys. Res., 73, 907-930, 1968.

Colburn, D. S., R. G. Currie, J. D. Milhalov, and C. P. Sonnett,
Diamagnetic Solar-Wind Cavity Discovered Behind Moon, Science,
158, 1040-1042, 1967.

Coleman, P. J., Jr., Turbulence, Viscosity, and Dissipation
in the Solar-Wind Plasma, Astrophys. J., 153, 371-388, 1968.

Dessler, A. J., Ionizing Plasma Flux in the Martian Upper
Atmosphere, paper presented at Conference on Atmospheres
of Mars and Venus, Tucson, Arizona, 1967.

Eckhardt, D. H., Geomagnetic Induction in a Concentrically
Stratified Earth, J. Geophys. Res., 68, 6273-6278, 1963.

England, A. W., G. Simmons, and D. Strangway, Electrical
Conductivity of the Moon, J. Geophys. Res., 73, 3219-3226,
1968.

Fairfield, C. H. and N. F. Ness, Magnetic Field Measurements
with IMP 2 Satellite, J. Geophys. Res., 72, 2379-2402, 1967.

Morse, P. M. and H. Feshbach, Methods of Theoretical Physics,
Part II, Chapter 13, McGraw-Hill, New York, 1953.

Muller, P. M., and W. L. Sjogren, Mascons: Lunar Mass
Concentrations, Science, 161, 680-684, 1968.

Ness, N. F., Simultaneous Measurements of the Interplanetary
Field, J. Geophys. Res., 71, 3319-3324, 1966.

Ness, N. F., K. W. Behannon, C. S. Scearce, and S. C. Cantarano,
Early Results from the Magnetic Field Experiment on Lunar
Explorer 35, J. Geophys. Res., 72, 5769-5778, 1967.

Sonnett, C. P., Modulation and Sampling of Hydromagnetic
Radiation, Space Res., 6, 280-322, 1966.

Siscoe, G. L., L. Davis, Jr., P. J. Coleman, Jr., E. J. Smith,
and D. E. Jones, Power Spectra and Discontinuities of the
Interplanetary Magnetic Field: Mariner 4, J. Geophys. Res.,
73, 61-82, 1968.

References (Contd.)

Stratton, J. A., Electromagnetic Theory, Chapter 7, McGraw-Hill, New York, 1941.

Wilcox, J. M. and N. F. Ness, Quasi-Stationary Corotating Structure in the Interplanetary Medium, J. Geophys. Res., 70, 5793-5805, 1965.

BELLCOMM, INC.

APPENDIX

          We present here the derivation of the vector Helmholtz
equation and its solution for a spherical geometry. The mathe-
matical procedure is abstracted from Stratton (1941) and Morse
and Feshbach (1953), and these works may be referred to for a
more detailed and complete discussion. Our method of solution
parallels that of Eckhardt (1963), who studied induction in the
earth using a layered model for the electrical conductivity.

          It is most convenient to treat the time dependence of
Maxwell's equations by a superposition of harmonic solutions.
Accordingly, we seek solutions which have a time variation $e^{-i\omega t}$,
and, upon combining the two curl equations and assuming Ohm's
law, $\underline{J} = \sigma \underline{E}$, to be valid, we arrive at

$$\nabla \times \nabla \times \underline{E} = k^2 \underline{E} \quad , \tag{A.1}$$

where

$$k^2 = i\mu\sigma\omega + \mu\epsilon\omega^2 \quad . \tag{A.2}$$

Any vector may be decomposed into an irrotational and a sole-
noidal component. Therefore we take $\underline{E} = \underline{E}_{irrot} + \underline{E}_{sol}$, where
$\nabla \times \underline{E}_{irrot} = 0$ and $\nabla \cdot \underline{E}_{rot} = 0$, and from (A.1) we see that if
$k^2 \neq 0$, then $\underline{E}_{irrot} = 0$. Consequently $\underline{E} = \underline{E}_{sol}$, and upon using
the vector identity $\nabla \times \nabla \times \underline{E} = \nabla(\nabla \cdot \underline{E}) - \nabla^2 \underline{E}$, we establish that
the electric field satisfies the vector Helmholtz equation

$$\nabla^2 \underline{E} + k^2 \underline{E} = 0 \quad . \tag{A.3}$$

          Knowing $\underline{E}$, the magnetic field is determined by the
Maxwell equation

$$\underline{B} = -\frac{i}{\omega} \nabla \times \underline{E} \quad . \tag{A.4}$$

Appendix (Contd.)

If we assume that the conductivity $\sigma(r)$ is constant except for a finite number of discontinuities at radii r_1, r_2, $\cdots$, this assumption being appropriate to a layered lunar model, then (A.3) is valid in each layer, with k^2 a different constant in each layer. The solutions in the various layers are matched uniquely by the use of the usual boundary conditions on $\underline{B}$ and $\underline{E}$.

Morse and Feshbach use a heuristic approach to construct the general solution of (A.3) by utilizing techniques suggested by the study of the scalar Helmholtz equation

$$\nabla^2 \psi + k^2 \psi = 0 \quad . \tag{A.5}$$

It can be verified by direct substitution that in a spherical coordinate system, three independent solutions of (A.3) are

$$\underline{E} = \underline{L} = \nabla \psi \quad , \tag{A.6}$$

$$\underline{E} = \underline{M} = \nabla \times (\underline{r}\psi) \quad , \tag{A.7}$$

$$\underline{E} = \underline{N} = \frac{1}{k} \nabla \times \underline{M} = \frac{1}{k} \nabla \times \nabla \times (\underline{r}\psi) \quad , \tag{A.8}$$

where the ψ's are solutions of (A.5) and $\underline{r}$ is the position vector. A linear superposition of (A.6) - (A.8) constitutes the general solution of (A.3).

In spherical coordinates, the most general solution of (A.5) which is independent of the azimuthal angle ϕ and is a non-singular function of the polar angle θ is

$$\psi = \sum_{n=0}^{\infty} \psi_n(r,\theta) = \sum_{n=0}^{\infty} [\alpha_n j_n(kr) + \beta_n y_n(kr)] P_n(\cos\theta)$$

where $j_n(z)$ and $y_n(z)$ are the spherical Bessel functions, $P_n(\cos\theta)$ are the Lengendre polynomials, and α_n and β_n are

Appendix (Contd.)

constants. Now if $k^2 \neq 0$, the condition $\nabla \cdot \underline{E} = 0$ requires $\underline{L} = 0$, and the general solution of (A.3) becomes

$$\underline{E} = + i \frac{\omega}{k} \sum_{n=0}^{\infty} \left(a_n \underline{M}_n + b_n \underline{N}_n \right) \quad , \tag{A.9}$$

where $\underline{M}_n$ and $\underline{N}_n$ are obtained by substituting ψ_n for ψ in (A.7) and (A.8), respectively. Then from (A.4) we find

$$\underline{B} = \sum_{n=0}^{\infty} \left(a_n \underline{N}_n + b_n \underline{M}_n \right) \tag{A.10}$$

where we have used (A.1), (A.7), and (A.8).

The $\underline{M}$ and $\underline{N}$ solutions have a particularly simple interpretation when they are independent of the azimuthal angle ϕ. If we use (A.5), (A.7) and (A.8) to evaluate the components of $\underline{M}$ and $\underline{N}$ in this case, we find

$$M_r = 0 \qquad , \quad M_\theta = 0 \qquad , \quad M_\phi = - \sum_{n=0}^{\infty} \frac{\partial \psi_n}{\partial \theta} \quad ; \tag{A.11}$$

$$N_r = \sum_{n=1}^{\infty} \frac{n(n+1)}{kr} \psi_n \quad , \quad N_\theta = \frac{1}{kr} \sum_{n=0}^{\infty} \frac{\partial^2 (r\psi_n)}{\partial r \partial \theta} \quad , \quad N_\phi = 0 \quad . \tag{A.12}$$

Hence $\underline{N}$ gives the poloidal magnetic field, and $\underline{M}$ the toroidal magnetic field.

To determine the electromagnetic field in the lunar interior we must specify boundary conditions at the lunar surface. A properly posed boundary value problem requires that N_r and M_ϕ be given at the surface. The former derives from the continuity of the normal component of the magnetic field, B_r, and determines the poloidal magnetic field, while the latter follows from the continuity of the tangential component of the electric field, E_θ, and determines the toroidal magnetic field.

Appendix (Contd.)

       The form of the magnetic source field allows only
the poloidal magnetic field solution, (B_r, B_θ). The toroidal
field B_ϕ is zero above the lunar surface, but since a surface
current J_θ can exist, e.g., due to the day-night asymmetry,
the toroidal field is not necessarily zero in the lunar inter-
ior. B_ϕ vanishes identically only if $E_\theta = 0$ over the entire
lunar surface.

BELLCOMM, INC.

DISTRIBUTION LIST

NASA Headquarters

Messrs. R. J. Allenby/MAL
W. O. Armstrong/MTX
P. E. Culbertson/MLA
R. J. Green/MAL
E. W. Hall/MTG
D. P. Hearth/SL
T. A. Keegan/MA-2
R. L. Lohman/MTY
M. A. Mitz/SL
W. T. O'Bryant/MAL
D. G. Rea/SL
A. W. Schardt/SG
L. R. Scherer/MAL
A. D. Schnyer/MTV
J. W. Wild/MTE
D. U. Wise/MAL

Ames Research Center

D. S. Colburn/SSE
L. Roberts/M (2)
C. P. Sonett/SS (3)
J. R. Spreiter/SST

Goddard Space Flight Center

J. P. Heppner/612
G. D. Mead/641
N. F. Ness/612
D. A. Stern/641
D. J. Williams/611

Manned Spacecraft Center

W. N. Hess/TA
J. L. Modisette/RG

Jet Propulsion Laboratory

C. W. Snyder

Cornell University

T. Gold

Southwest Center for Advanced Studies

F. S. Johnson/DASS

Massachusetts Institute of Technology

H. S. Bridge
T. R. Madden
F. Press
G. Simmons

National Radio Astronomy Observatory

J. W. Findlay

Princeton University

R. A. Phinney

Rice University, Houston, Texas

A. J. Dessler

Stanford University

W. Shockley

United States Geological Survey

H. Masursky
E. Shoemaker

The University, Newcastle-upon-Tyne, England

S. K. Runcorn

California Institute of Technology

B. C. Murray
L. Davis, Jr.

University of California at Berkeley

L. Alvarez
F. S. Mozer
C. H. Townes
S. Ward

BELLCOMM, INC.

University of California
at Los Angeles
Mr. P. J. Coleman, Jr.

University of California
at San Diego
Messrs. J. Arnold
       H. Urey

University of Iowa
    J. A. Van Allen

University of Kansas
    D. B. Beard

University of New Hampshire
    L. J. Cahill

Bellcomm, Inc.
    F. G. Allen
    G. M. Anderson
    A. P. Boysen, Jr.
    D. A. Chisholm
    C. L. Davis
    D. A. DeGraaf
    J. P. Downs
    R. E. Gradle
    D. R. Hagner
    P. L. Havenstein
    N. W. Hinners
    B. T. Howard
    D. B. James
    J. Kranton
    M. Liwshitz
    H. S. London
    K. E. Martersteck
    R. K. McFarland
    J. Z. Menard

Bellcomm, Inc. (Cont'd)
    G. T. Orrok
    I. M. Ross
    F. N. Schmidt
    R. V. Sperry
    C. M. Thomas
    W. B. Thompson
    C. C. Tiffany
    J. W. Timko
    R. L. Wagner
    J. E. Waldo
All members, Division 101
Department 2015
Central Files
Department 1024 File
Library